Characterisation of a large area silicon photomultiplier

A. Nagai[a,*], C. Alispach[a], A. Barbano[a], V. Coco[b], D. della Volpe[a], M. Heller[a], T. Montaruli[a], S. Njoh[a], I. Troyano-Pujadas[a], Y. Renier[a]

[a]*Départment de physique nucléaire et corpusculaire, Université de Genève, 24 Quai E. Ansermet, CH-1211, Switzerland*
[b]*European Organization for Nuclear Research CERN, 1, Esplanade des particules, CH-1211 Genve 23, Switzerland*

arXiv:1810.02275v4 [physics.ins-det] 9 Jan 2020

Abstract

This work illustrates and compares some methods to measure the most relevant parameters of silicon photo-multipliers (SiPMs), such as photon detection efficiency as a function of over-voltage and wavelength, dark count rate, optical cross-talk, afterpulse probability. For the measurement of the breakdown voltage, V_{BD}, several methods using the current-voltage IV curve are compared, such as the "IV Model", the "relative logarithmic derivative", the "inverse logarithmic derivative", the "second logarithmic derivative", and the "third derivative" models. We also show how some of these characteristics can be quite well described by few parameters and allow, for example, to build a function of the wavelength and over-voltage describing the photodetection efficiency. This is fundamental to determine the working point of SiPMs in applications where external factors can affect it.

These methods are applied to the large area monolithic hexagonal SiPM S10943-2832(X), developed in collaboration with Hamamatsu and adopted for a camera for a gamma-ray telescope, called the SST-1M. We describe the measurements of the performance at room temperature of this device. The methods used here can be applied to any other device and the physics background discussed here are quite general and valid for a large phase-space of the parameters.

Keywords: SiPM, MPPC, *PDE*, V_{BD}, cross-talk, dark count rate, afterpulses, triggering probability
2010 MSC: 00-01, 99-00

1. Introduction

In the last few years the interest in solid state photodetectors has grown significantly. In particular, SiPMs [1] have replaced traditional photo-multiplier tubes (PMTs) in many applications. As a matter of fact, they are very compact, robust, lightweight, insensitive to magnetic fields and work at temperatures that span a wide range from cryogenics to beyond room temperature. Their operating parameters are stable across devices of the same type thanks to the high level of uniformity achieved by the solid state technology production technique. Also the absence of aging caused by the integrated light over time, makes them particularly tailored for ground-based astrophysics [1], where they can be operated even in the presence of high background light level, thus increasing the duty cycle and then the physics reach of experiments [2].

The University of Geneva and a Consortium of Polish and Czech Institutions have proposed and built a single mirror small size telescope (SST-1M) for the Cherenkov Telescope Array (CTA), equipped with a SiPM-based camera. To achieve the desired performance with the chosen optics, a mirror of 4 m diameter, the camera of the SST-1M is composed by 1296 pixels, each of an angular opening of about 0.24°. This translates into a pixel linear size of about 2.32 cm (more details on camera and its design and performances can be found in ref. [3]).

In order to have a spatial uniform response of the camera, the pixels should have a circular shape to ensure equal distance between pixel centres in every direction. The hexagon is the best possible shape to achieve this uniformity with minimum dead space. The pixel size to achieve the required angular resolution is achieved through a large SiPM coupled with light funnel. A light funnel, approaching the ideal Winston cone geometry, was designed by the University of Geneva group to be coupled to SiPMs and achieve the desired pixel size. The light funnel has hexagonal shape and has a compression factor of about six [4]. Its internal surface is coated in order to maximise reflection of UV Cherenkov light produced by the cosmic rays when traversing the atmosphere, and also to have a good reflectivity for light with a direction almost parallel to cone surface.

The Winston cone geometry, on the other side, imposes to have the same shape at entrance and exit side and then an hexagonal sensor was needed. This was developed by the University of Geneva group in cooperation with the Hamamatsu company (Hamamatsu S10943-2832(X)). The main characteristics of the sensor are detailed in Tab. 1. The sensor area is around 93.6 mm^2 with a linear dimension of 10.4 mm flat-to-flat. It ranks among the world's largest monolithic sensor. The large area can be a limiting factor in many application. As matter of fact, the capacitance and the dark-count rate (DCR) are proportional to SiPM area. Hence, larger devices tend to have longer output signals and be more noisy. However, as shown by the SST-1M camera [3], with the proper electronics, such a large device can achieve the desired performances in specific applications.

*Corresponding author
Email address: Andrii.Nagai@unige.ch (A. Nagai)
[1]Hamamatsu adopted the name Multi-Pixel Photon Counters or MPPCs

This work reports on the characterization studies done to validate the design and verify the performances of the SST-1M new sensor type.

Nr. of channels	4
Cell size	$50 \times 50\ \mu m^2$
Nr of cells (per channel)	9210
Fill Factor	61.5%
DCR (@V_{op} per channel)	2.8-5.6 MHz
$C_{\mu cell}$ (@ V_{op} per channel)	85 fF
Cross-talk (@V_{op} per channel)	10%
V_{BD} Temp. Coeff.	54 mV/C°
Gain (@V_{op} per channel)	1.49×10^6

Table 1: S10943-2832(X) SiPM main characteristics provided by the producer at T = 25 °C. $V_{op} = V_{BD} + 2.8$ V.

2. The Hamamatsu S10943-2832(X) SiPM

The SiPM S10943-2832(X), shown in Fig. 1, has been designed in collaboration with Hamamatsu and is based on the so called LCT2 (Low cross-talk) technology available when the camera design was done. Hamamatsu has further improved this technology (LCT5 or LVR) and offers now better performance. It is worth to mention that the hexagonal shape can be obtained using any Hamamatsu μcell standard technology and size, through a dedicated photo-mask. Currently, we evaluate that the slightly higher DCR of LCT2 does not impact significantly performances of camera if appropriately calibrated. Actually, dark counts are useful for in-situ calibrations and then a further reduction of this rate increases the time needed to accumulate the statistics needed for precise calibrations.

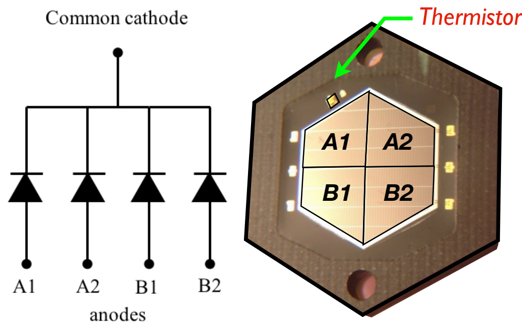

Figure 1: Picture of the Hamamatsu S10943-2832(X) SiPM (right) and its electric equivalent model (left). On the sensor package also a NTC temperature probe is present. This is used to monitor the temperature variation affecting parameters as DCR or $V_{breakdown}$, for which a real-time correction can be applied to keep the working point stable [5].

The sensor capacitance is directly related to its active area and this has an impact on the signal recharge time. In this case,

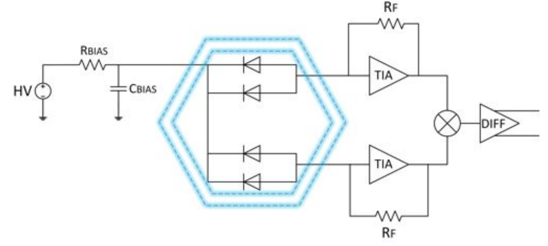

Figure 2: SiPM polarisation scheme and pre-amplifier topology used to sum up its four channels.

signals would have typical duration of about hundred ns, a too long time for the desired bandwidth of 250 MHz. This frequency has been chosen taking into account the typical time duration of atmospheric showers induced by gamma-rays and cosmic rays. To reduce the effect of the capacitance, the sensor has four independent anodes and a common cathode as shown in Fig. 1. This configuration allows to readout the 4 channels independently but there is a single bias for the whole sensor. Nonetheless, in order to achieve the desired bandwidth, a shaping of the signal is needed.

To address this features, we developed in house the pre-amplification chain based on off-the-shelf components. The solution adopted [5] is a trans-impedance amplifier topology with low noise amplifiers (OPA846) as it can achieve the required events rate with the best signal-to-noise ratio and gain/bandwidth ratio. As shown in Fig. 2, the four channels are summed by two in order to reduce the equivalent capacitance and pulse length. The summed signals are further summed up in a differential amplifier, which feeds the output signal into the digital readout system.

Another important characteristic of the camera architecture is the fact that the front-end and the digital readout are DC coupled. This is important for gamma-ray astronomy, where Moon light and human-induced light and their reflections are a relevant background. As a matter of fact, the Night Sky Background (NSB) contributes to the determination of the real working point of the device, relevant to correctly extract the number of photons from the signal.

3. Static characterisation

All the laboratory measurements (i.e. static, dynamic and optical) are performed at room temperature T = 25 °C at the premises of IdeaSquare[2] at CERN, where an experimental setup has been developed. The static characterization (i.e. reverse and forward current-voltage (IV) curves), is performed using a Keithley 2400 [6] pico-ammeter for bias supply and current measurements.

3.1. Forward IV characterization

The forward IV characteristic curve of the SiPM, shown in Fig. 3, exhibits a very small increase of the current when the

[2] http://ideasquare.web.cern.ch

polarization voltage, V_{bias}, is below the threshold value and a linear rapid current increase with V_{bias} above this threshold. A physical interpretation of this behaviour can be attempted starting from the ideal Shockley law [7], which expresses the forward current flowing I^d through a *p-n* diode as:

$$I^d = I^d_s \left[exp\left(\frac{V_j}{\eta V_T}\right) - 1 \right], \quad (1)$$

where I^d_s is the diode reverse bias saturation current, V_j is the voltage across the junction, V_T is the thermal voltage and η is the ideality factor. The voltage V_j is the difference between the applied voltage V_{bias} and the voltage drop across the neutral region and the ohmic contacts on the two sides of the junction:

$$V_j = V_{bias} - I^d \cdot R_s \quad (2)$$

where usually $R_s \simeq 100\ \Omega$.

Replacing V_j by V_{bias} in Eq. 1, we obtain:

$$V_{bias} = \eta V_T \left[\ln\left(\frac{I^d}{I^d_s} + 1\right) \right] + I^d \cdot R_s\,. \quad (3)$$

The SiPM is an array of $N_{\mu cell}$ micro-cells (μcells), which are SPADs (single photon avalanche diode). Each μcell can be represented by a diode connected in series with a quenching resistor R_q[3]. Eq. 3 applies to each single μcell but requires the addition of the voltage drop caused by the presence of a quenching resistance R_q. Then for a full SiPM device with $N_{\mu cell}$ connected in parallel, Eq. 3 becomes:

$$V_{bias} = \eta V_T \left[\ln\left(\frac{I}{I_s} + 1\right) \right] + I\frac{(R_s + R_q)}{N_{\mu cell}}\,. \quad (4)$$

where I_s is the SiPM reverse bias saturation total current and I is the forward total current flowing through it.

The last term of Eq. 4 becomes dominant when the current is high ($I/N_{\mu cell} > 5\ \mu$A). In this regime, $R_s + R_q$ can be extracted from a linear fit of the forward IV characteristic curve in Fig. 3:

$$R_q + R_s = \frac{N_{\mu cell}}{b} \underset{|R_q >> R_s|}{\simeq} R_q\,. \quad (5)$$

where b is the slope parameter extracted by the linear fit (red line in Fig. 3). Also, b can be calculated as $b = \frac{dI}{dV_{bias}}$. For this SiPM, the fit gives $R_q = 182.9 \pm 0.3$ (stat.) ± 31 (sys.) kΩ. The systematic uncertainty comes from the fact that I does not increase linearly with V_{bias}. This can be seen from the bottom part of Fig. 3, showing $Ratio = \left(I_{data} - I_{fit}\right)/I_{data}$ and $\frac{dI}{dV_{bias}}$. It is calculated as:

$$\sigma^{R_q}_{sys.} = 0.5 \cdot \left(\frac{N_{\mu cell}}{b_{1.6V}} - \frac{N_{\mu cell}}{b_{2.5V}}\right). \quad (6)$$

where $b_{1.6V}$ and $b_{2.5V}$ are two slopes calculated at V_{bias} of 1.6 V and 2.5 V respectively.

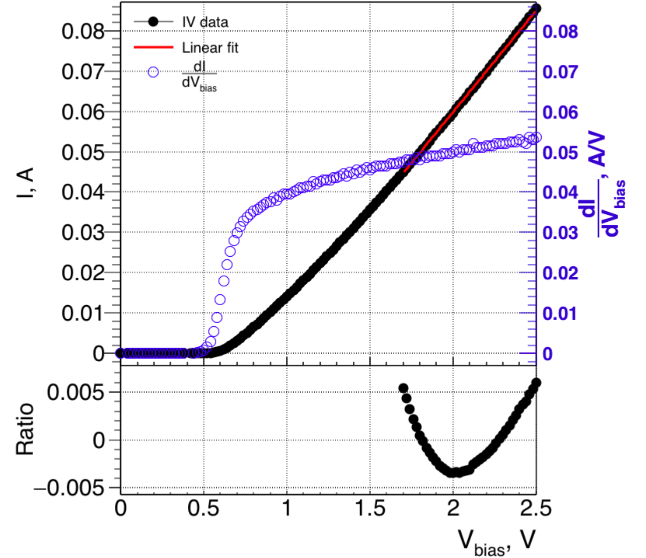

Figure 3: The forward IV characteristic and its derivative of the Hamamatsu S10943-2832(X) SiPM. The linear fit (red line) is superimposed to data points. In the bottom pane is shown the $Ratio = \left(I_{data} - I_{fit}\right)/I_{data}$.

3.2. Reverse IV characterisation

The current flowing in the SiPM, when not illuminated, depends on the available free carriers. The Shockley-Read-Hall (SRH) [8, 9] effect is the dominant one in semiconductors and it is also the main contribution to the bulk dark current. It describes the generation and recombination of electron-hole pairs due to the trapping effect of impurities in the lattice (for this also called trap-assisted recombination), as well as band-to-band tunneling effects. In addition the carriers generation rate can be enhanced by reduction of activation energy due to the Poole-Frenkel effect [10].

In the reverse IV characteristic curve of the SiPM, shown in Fig. 4, two zones are identified, corresponding to different regimes:

(1) the "Linear" regime (pre-breakdown), corresponding to V_{bias} below the breakdown voltage (V_{BD}), where the current increases slowly with V_{bias}. This dark current is due to the surface current and the bulk dark current due to the free carriers.

(2) the "Geiger" regime (post-breakdown), corresponding to V_{bias} above V_{BD} where the current increases much faster with V_{bias}. This trend is due to the Geiger avalanche created by the free carriers generated by ionization. Primary free carriers, which trigger an avalanche, are usually created, due to the SRH thermal generation enhanced by Poole-Frenkel effect and tunnelling, but also to other associated effects as afterpulsing, prompt cross-talk and delayed cross-talk.

[3] The μcell works in Geiger-Avalanche mode meaning that when a photon is absorbed, an electron-hole pair is created and the high electric field in the junction starts charge multiplication, which produces an avalanche. If the field is not reduced, the charge avalanche is stationary and leads to thermal destruction of the device. By adding a resistor in series to the μcell, a voltage drop is produced by the current induced by the charge avalanche when flowing into the resistor. This drop reduces the field across the device thus quenching the avalanche. For this reason the SiPM are also referred to as an array of G-APDs - Geiger-Avalanche Photo-Diodes.

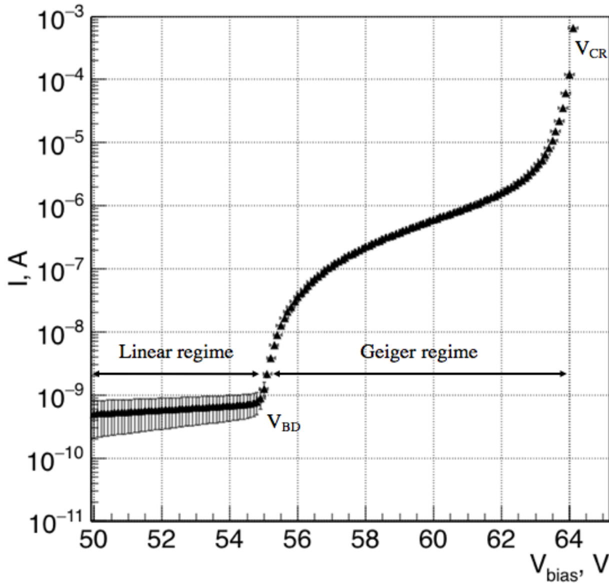

Figure 4: The reverse IV characteristic data points of the Hamamatsu S10943-2832(X) SiPM. Two different regions can be distinguished: *pre − breakdown* and *post − breakdown*.

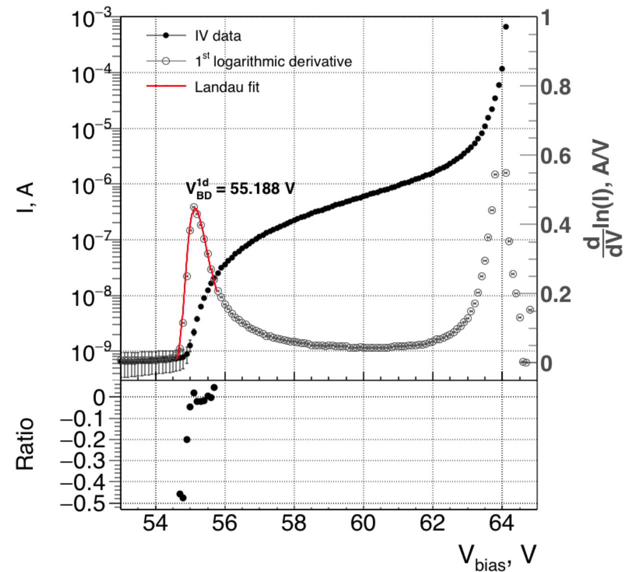

Figure 5: The reverse IV characteristic data points and its logarithmic derivative. A V_{BD}^{1d} = 55.188 V is extracted from the fit of the data (red line) with a Landau function. Also, the *Ratio* $= \left(\frac{d}{dV}\ln(I) - I_{fit}\right) / \frac{d}{dV}\ln(I)$ is shown at the bottom of the figure.

The breakdown voltage V_{BD} of a SiPM device represents the voltage above which the electrical field inside the depleted region of a μcell is high enough that any free carrier (created by an absorbed photon or by a thermally generated carrier) can trigger an avalanche. It marks, then, the transition between the two regimes and that is why it represent one of the most important parameter to determine.

The reverse IV measurements is commonly used for fast calculation of V_{BD} using different methods such as the "relative logarithmic derivative" [11], the "inverse logarithmic derivative" [12], the "second logarithmic derivative" [13], the "third derivative" [14] and "IV Model" methods [15, 16].

In the "relative logarithmic derivative" the breakdown voltage can be calculated [17] as the voltage where $\frac{d}{dV_{bias}}\ln(I) = \frac{n}{V_{bias}-V_{BD}}$ diverges, where n is the model constant which determine the shape of the reverse IV. Clearly, this divergence is not observed in the experimental data, being a non-physical state. Therefore, from this method one can extract V_{BD}^{1d}, a quantity proportional to V_{BD}, as the voltage at which the "relative logarithmic derivative" has a local maximum, for example by fitting the region around V_{BD} with a peaked and skewed function. In our case, we chose a Landau function (see Fig. 5).

The "inverse logarithmic derivative" $1/\frac{d}{dV_{bias}}\ln(I)$ increases linearly with V_{bias} above the V_{BD} (See Fig. 6). Assuming that this behaviour does not change near the breakdown region, the breakdown voltage $V_{BD}^{1dinv.}$ can be extracted as the voltage at which the "inverse logarithmic derivative" is equal to zero, i.e. the intersection with the x-axis of the fitted line above V_{BD}.

The "second logarithmic derivative" method [13, 18] is commonly used for the V_{BD} determination. Here, V_{BD}^{2d} is calculated as the voltage corresponding to the maximum of the second derivative, as shown in Fig. 7. However, we observe that the Gaussian fit does not describe the data well. Therefore, this method determines a systematic error in the absolute value of V_{BD}.

The "third derivative" method [19, 14] assumes two separate breakdown voltages: the "turn-on" $V_{BD}^{3d\ turn-on}$ and "turn-off" $V_{BD}^{3d\ turn-off}$ voltages. $V_{BD}^{3d\ turn-on}$ defines the regime in which a μcell initiates an avalanche and the current is related to the avalanche triggering probability P_G. $V_{BD}^{3d\ turn-off}$ is the voltage at which the quenching of the avalanche starts and the current is related to charge production. Following the prescription in Ref. [14], we find 54.65 V and 55.45 V for $V_{BD}^{3d\ turn-off}$ and $V_{BD}^{3d\ turn-on}$, respectively (see Fig. 8).

To overcome the limitation of all the methods shown so far, a model of the reverse IV curve has been proposed [15, 16]. According to this "IV Model", different SiPM working regimes can be identified in the IV curve, as shown in Fig. 9. As in Fig. 4 the "Linear" region (1) is below V_{BD}, while here the "Geiger" region above V_{BD}, is split in four different regions: the "just-above" (breakdown), "transition", "far-above" and "post-second breakdown" zones.

This model can describe the IV over the full working range of SiPM and therefore it can be used not only to determine breakdown voltage $V_{BD}^{IV-Model}$, but also to determine other SiPM parameters such as working range or Geiger probability P_G when the IV is measured under light illumination. Here we use the procedure described in Ref. [15], and we obtain a $V_{BD}^{IV-Model}$ = 54.799 V.

The systematic uncertainty on all these measurements is given by the:

- voltage source accuracy, which has been determined as

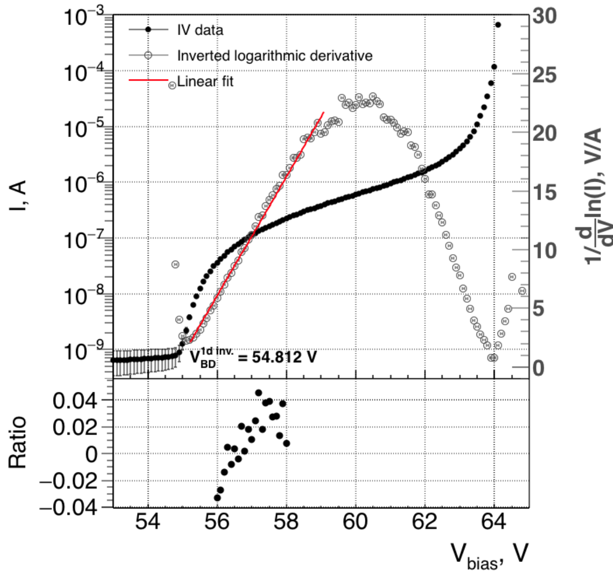

Figure 6: The reverse IV characteristic data points and its inverted logarithmic derivative. A value of $V_{BD}^{1dinv.}$ = 54.812 V is determined as intercept of the x-axis of the right scale and the fitted inverted logarithmic derivative (red line). Also, the $Ratio = \left(1/\frac{\mathrm{d}}{\mathrm{d}V}\ln(I) - I_{fit}\right) \div 1/\frac{\mathrm{d}}{\mathrm{d}V}\ln(I)$ is shown at the bottom.

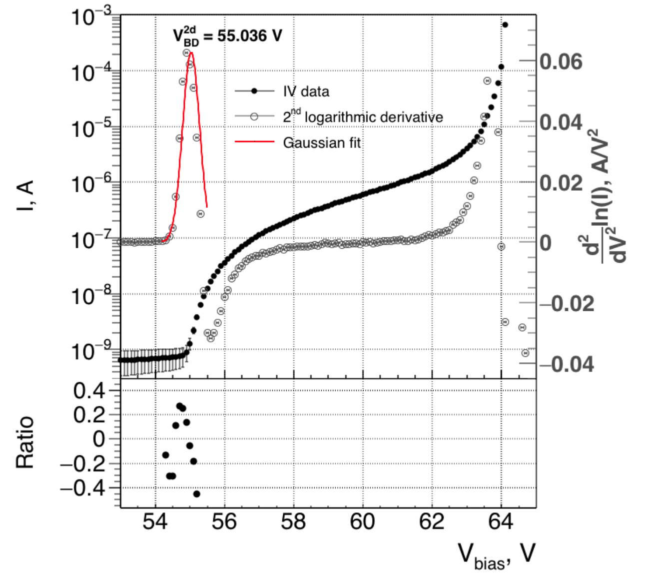

Figure 7: The reverse IV characteristic data points and its second logarithmic derivative curve. The V_{BD}^{2d} = 55.036 V is extracted from the fit of the peak. Also, the $Ratio = \left(\frac{\mathrm{d}^2}{\mathrm{d}V^2}\ln(I) - I_{fit}\right) \div \frac{\mathrm{d}^2}{\mathrm{d}V^2}\ln(I)$ is shown at the bottom of the figure.

suggested by the producer [6] as:

$$\sigma_{sys.} = V_{BD} \cdot 0.02\% + 24\mathrm{mV} \sim 35\mathrm{mV} \quad (7)$$

.

- the model assumptions made to approximate the IV curve with a simple equation:
  - as already noted, divergence to infinity of the reverse IV for the "relative logarithmic derivative" and for the "inverse logarithmic derivative" cannot physically observed;
  - "second logarithmic derivative" and "third derivative" methods do not fit perfectly experimental data;
  - the "IV Model" does not describe the experimental data near $V_{BD}^{IV-Model}$ and V_{CR}. As a matter of fact, a SiPM biased below V_{BD} works like an avalanche photodiode and this regime is not included in the IV Model (for more details see Ref. [16]). Additionally, following Ref. [20], the V_{BD} value is subject to statistical fluctuations due to Geiger avalanche statistical fluctuations. On the other hand, the difference near V_{CR} is related to the voltage drop on R_q.

In Fig. 10, the values of V_{BD} obtained using the described methods are compared. They are spread over a range of less than 1 V. In general, the "inverse logarithmic derivative" or "second logarithmic derivative" methods provide the most stable and straightforward results, and provide a reasonable estimate of V_{BD}. Therefore, those methods are used when many SiPM devices should be characterized or compared, as for example in quality assurance procedures. However, for the full characterization of a device, the "IV model" should be used, as it can provide the most complete description of the reverse IV. This is the optimal method when design and tuning of front-end electronics is needed or to compare performance of different devices. Moreover, as will be shown in Sec. 5.2, the "IV Model" method can also provide the relative photodetection efficiency (PDE) of a device.

Fig. 10 also shows the value of the breakdown voltage as determined with a measurement done with light, which will be described later in Sec. 4.

4. Dynamic characterisation

For the dynamic measurements presented here (also refereed further as AC measurements), instead of the standard preamplification topology used in the real camera [5](see Fig. 2), each SiPM channel is connected to an operational amplifier OPA846 and readout independently. The SiPM device is illuminated with low intensity light of different wavelengths (e.g. 405 nm, 420 nm, 470 nm, 505 nm, 530 nm and 572 nm) produced by pulsed LEDs. For each operating voltage of the LED providing a certain light level, 10'000 waveforms are acquired on an oscilloscope and sampled at 500 MHz. Each one is 10 μs long. The signal used to pulse LEDs is produced by a pulse generator and it is also used to trigger waveform acquisition.

The readout window is adjusted in such a way to have the trigger signal in the middle of the waveform. i.e. at 5 μs from the window start, in order to have

- a "*Dark*" interval from 0 to 5 μs, when the device is operated in dark conditions. Only uncorrelated DCR enhanced

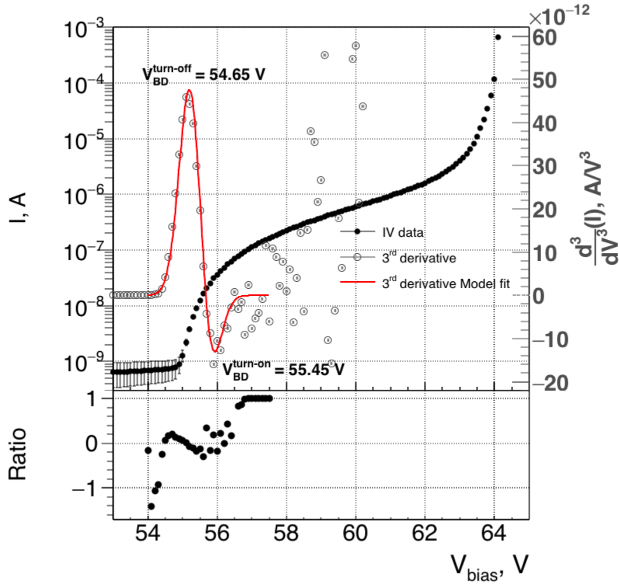

Figure 8: The reverse IV characteristic data points and its third derivative. The values of 54.65 V and 55.45 V is found for "turn-off" and "turn-on" V_{BD} from the fit of the curve. Also, the $Ratio = \left(\frac{d^3}{dV^3}(I) - I_{fit}\right) \div \frac{d^3}{dV^3}(I)$ is shown at the bottom of the figure.

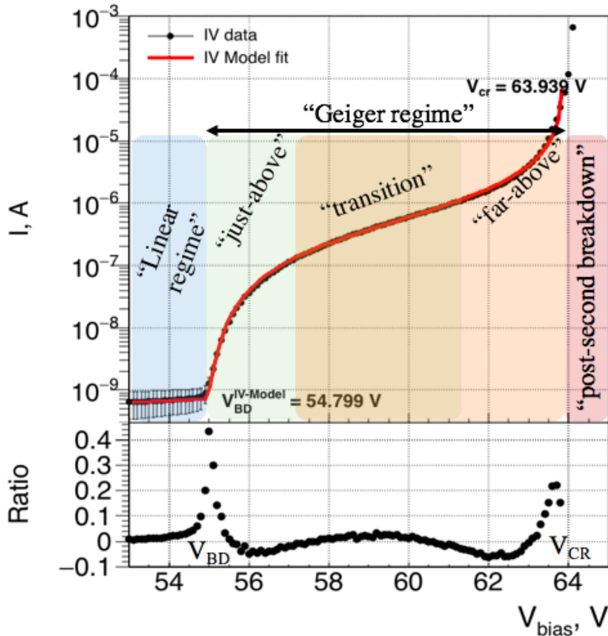

Figure 9: The reverse IV characteristic data points and its fit done with the "IV Model", from which a $V_{BD}^{IV-Model}$ of 54.621 V is extracted. The main regions ("pre-breakdown", 'just-above", "transition", "far-above" and "post-second breakdown") are highlighted with different colours. Also, the $Ratio = \frac{I_{data}-I_{fit}}{I_{data}}$ is shown at the bottom of the figure.

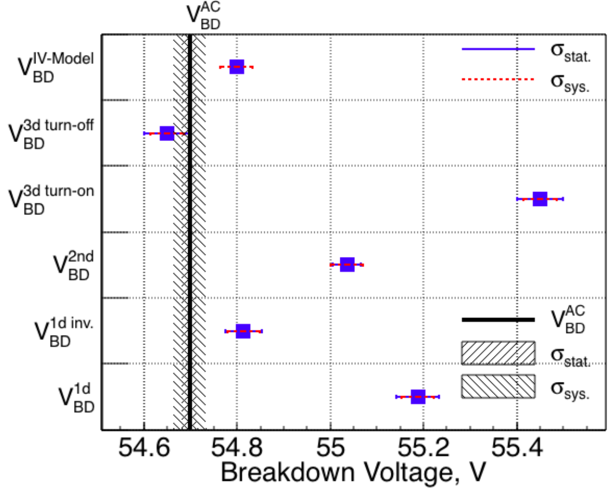

Figure 10: V_{BD} with statistics ($\sigma_{stat.}$) and systematic ($\sigma_{sys.}$) errors of the Hamamatsu S10943-2832(X) SiPM obtained form static and dynamic measurements.

by correlated noise, i.e. cross-talk (prompt and delayed) and afterpulses, are present (see Sec. 4.5 for more details);

- "*LED*" interval, from 5 to 10 μs, when the device is illuminated by LED light pulses. In this case, both signals pulses due to the light and uncorrelated SiPM noise pulses are present. Both types of pulses are further affected by SiPM correlated noise (i.e. prompt and delayed cross-talk and afterpulses).

Dark intervals are used to calculate the SiPM *Gain*, the breakdown voltage V_{BD}^{AC}, the dark count rate (*DCR*) and the optical cross-talk probability P_{XT}, while *LED* intervals are used to calculate the SiPM photon detection efficiency *PDE*. To measure the afterpulses probability P_{AP}, an additional data run was performed (See sec. 4.5.2).

The data acquisition system used for these measurements, consists of a transimpedance amplifier based on OPA846, an oscilloscope Lecroy 620Zi for the waveform acquisition (a bandwidth of 20MHz is used to reduce the influence of the electronic noise) and a Keithley 6487 to provide bias voltage to the SiPM. For each LEDs of different wavelengths, the over-voltage $\Delta V = V_{bias} - V_{BD}^{AC}$ is varied in the range 1 V $< \Delta V <$ 8 V, to cover the full working range of the device (see Sec. 3.2).

4.1. Automatic data analysis procedure

The acquired experimental data are analyzed with an automatic procedure developed in the ROOT Data Analysis Framework [4]. The waveforms acquired with the oscilloscope are used to create ntuples storing SiPM pulse templates. The steps of the analysis to determine the main features of pulses are the following:

- the construction of a template of a typical SiPM pulse shape (see Fig. 11) in a given working condition;

[4] https://root.cern.ch

- a pulse finding procedure to identify SiPM pulses (i.e. a single pulse or a train of pulses [5]) and their relative time spacing;
- a template subtraction to reconstruct only the SiPM pulses in a train of pulses.

The SiPM pulse characteristics, such as the baseline, time position and amplitude, rise time and decay time, charge Q, t_{before}[6] and t_{after}[7], are determined for different values of V_{bias}. More details on the developed analysis procedure can be found in the Ref.[21].

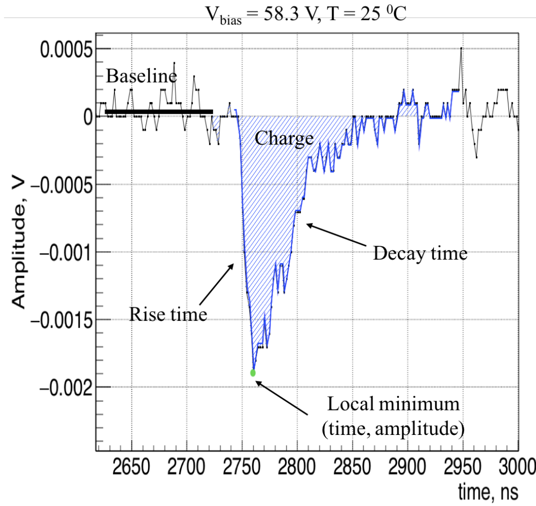

Figure 11: Typical SiPM pulse for a single photon equivalent (1 p.e.) on top of which its main characteristics are indicated.

4.2. SiPM Gain

The SiPM gain G is defined as the number of charges created by one avalanche in one $\mu cell$ and it can be expressed as:

$$G = \frac{Q}{e} = \frac{\left(C_{\mu cell} + C_q\right) \cdot \left(V_{bias} - V_{BD}^{AC}\right)}{e}, \quad (8)$$

where Q is the avalanche charge, $C_{\mu cell}$ and C_q are the $\mu cell$ and parasitic capacitance, respectively, and V_{BD}^{AC} is the breakdown voltage (more details are given in Sec. 4.3). The SiPM gain can be calculated from the time integration of the signals of a device:

$$G = \frac{Q}{e} = \frac{1}{G_{Amp} \cdot e} \cdot \frac{1}{R} \int (V(t) - BL)\, dt, \quad (9)$$

where G_{Amp} is the amplifier gain, R is the amplifier input impedance ($R = 50\ \Omega$), $V(t)$ is the pulse evolution over time and BL is the baseline. The gain of the OPA846 amplifier has strong frequency dependence. Therefore, it will be different for different SiPMs. However, in particularly for our SiPM device the G_{Amp} of 5.86 ± 0.04 was found. At a given V_{bias} and temperature the SiPM gain has Gaussian shape as shown in [22]. Therefore, gain errors were calculated as the errors of the mean. As can be seen in Fig. 12, the gain increases linearly with V_{bias} as expected from Eq. 8.

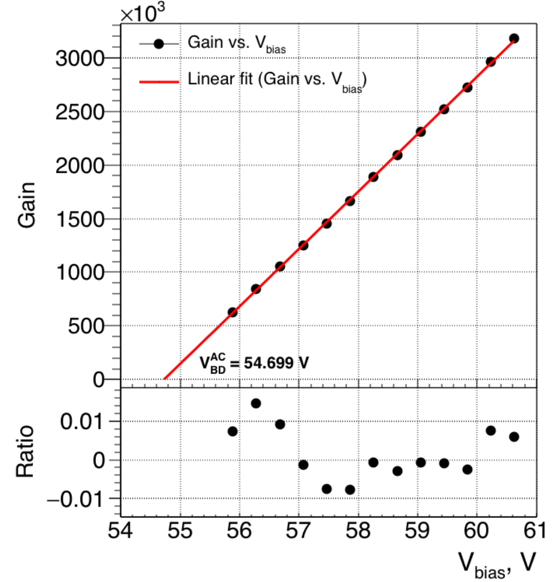

Figure 12: SiPM gain vs. V_{bias} for the Hamamatsu S10943-2832(X). The V_{BD} of 54.699 V is found at the intersection of the linear fit with the x-axis. Also the ratio, defined as the difference between the experimental data and the fit function values divided by the experimental data, is shown.

4.3. Breakdown Voltage

From the curve of the gain as a function of V_{bias} (Fig. 12), the breakdown voltage V_{BD}^{AC} can be determined as the value where $G = 0$ (see Eq. 8), i.e. extrapolating the linear fit to zero. The obtained value is $V_{BD}^{AC} = 54.699 \pm 0.017$ (stat.) $\pm$ 0.035 (sys.) V. The comparison between this value and those obtained from reverse IV curve static methods (see Sec. 3.2) is shown in Fig. 10. We can observe significant differences between the dynamic measurement and the static ones, except for the $V_{BD}^{3dturn-off}$ obtained with the 3rd derivative method. The V_{BD}^{AC} and $V_{BD}^{turn-off}$ are equal within the uncertainties. However, for all other breakdown voltages, the V_{BD}^{AC} value is a few hundreds of mV smaller than V_{BD} from the IV methods. This discrepancy reflects the described limitation of some of the static methods. As it can be seen in Fig. 13, the IV static measurement is sensitive to the onset of the avalanche phenomenon and it determines the breakdown voltage, as defined by the fundamental papers of McIntyre (named as "turn-on" voltage) [23]. The *Gain* linearity dynamic method determines the voltage across the diode when the avalanche is quenched (named as "turn-off" voltage). The "turn-off" (i.e. V_{BD}^{AC} and $V_{BD}^{turn-off}$) is naturally lower than the "turn-on" (i.e. V_{BD}^{1d}, $V_{BD}^{1dinv.}$, V_{BD}^{2nd}, $V_{BD}^{3dturn-on}$ and $V_{BD}^{IV-Model}$), as shown in the Fig. 10).

[5] By single pulses here it is intended a SiPM signal separated by neighbouring pulses by a time interval longer than its recovery time, while train of pulses is a sequence of two or more signals within a time interval shorter than the SiPM recovery time.

[6] Time difference between the analyzed pulse and the previous one.

[7] Time difference between the analyzed pulse and the following one.

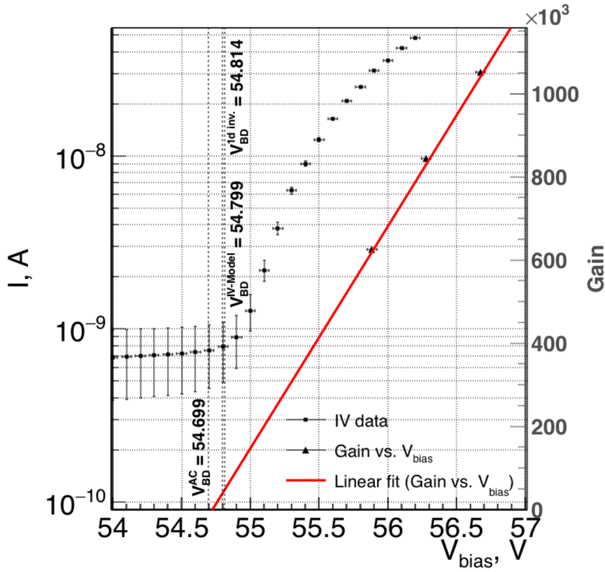

Figure 13: The zoom near V_{BD} region of the reverse IV curve with superimposed the linear fit of Gain vs. V_{bias} data from Fig. 12. Vertical lines indicate various breakdown voltages: V_{BD}^{AC}, $V_{BD}^{IV-Model}$ and $V_{BD}^{1dinv.}$

4.4. SiPM micro-cell capacitance and depletion depth

Combining Eq. 8 and Eq. 9, one can extract the device capacitance, which is the sum of the μcell $C_{\mu cell}$ capacitance and the parasitic C_q one. $C_{\mu cell}$ is related to μcell geometry, through the parallel plane capacitance equation:

$$C_{\mu cell} = \epsilon_0 \cdot \epsilon_{Si} \times \frac{A}{d}, \tag{10}$$

where $\epsilon_0 = 8.854 \times 10^{-14}$ F/cm is the vacuum permittivity, $\epsilon_{Si} = 11.9$ is the silicon dielectric constant, $A = (50 \times 50) \times 0.615\ \mu\text{m}^2$ is the active area reduced by the geometrical fill factor of 0.615 and d is the depletion thickness of the μcell. From this formula, the resulting depletion thickness is $d = 1.9\ \mu$m. This relationship between $C_{\mu cell}$ and the depletion thickness was studied with Silvaco TCAD[8] simulation of the capacitance-voltage characteristic of a diode structure similar to the SiPM microcell (i.e. p+/n/n-epi/n-substrate). We found agreement between simulated and calculated depletion thicknesses within 0.1 μm, corresponding to 5.2 % relative error.

4.5. SiPM noise and DCR

SiPM noise is a limiting factor for low-light level applications (from one to few photons) and various mechanisms contribute to it. Two main categories of noise can be identified: the *DCR* or primary uncorrelated noise, which is independent from light conditions, and the secondary or correlated noise.

At room temperatures, the *DCR* is dominated by thermal generation of carriers. When a SiPM is operated at high overvoltage ΔV and the electric field across the junction increases, the carriers can tunnel from the valence band to the conduction band through trap or defect states. In this case, the rate of thermally generated carriers is amplified by the trap-assisted tunnelling mechanism. In addition, the generation rate can be enhanced by the reduction of activation energy due to the Poole-Frenkel effect [10]. As the electric field increases, the tunnelling of electrons directly from the valence band into the conduction band increases. Therefore, at a given temperature, the *DCR* is determined by the rate of thermally generated carriers N_{car} and the probability that carriers trigger an avalanche (i.e. Geiger probability P_G). Consequently, a simple empirical formula for the *DCR* can be approximated as:

$$DCR = N_{car} \cdot P_G^{DCR} \cdot e^{b \cdot V_{bias}} \tag{11}$$

where b is a free parameter describing the increase of *DCR* with V_{bias} due to electrical field effects, P_G^{DCR} is the average Geiger probability for dark pulses. Following the Refs. [15] [24] the Geiger probability can be well expressed as:

$$P_G = 1 - e^{-P_{G_{Slope}} \cdot \Delta V} \tag{12}$$

where $P_{G_{Slope}}$ is the SiPM structural parameter, which determines the rate of increase of P_G with ΔV. $P_{G_{Slope}}$ depends on whether an electron or a hole initiates an avalanche (i.e. it detected light of some wavelength) and to some extent on the temperature [25] (See Sec. 5.3). Therefore, P_G^{DCR} can be approximated as:

$$P_G^{DCR} = 1 - e^{-P_{G_{Slope}}^{DCR} \cdot \Delta V} \tag{13}$$

where $P_{G_{Slope}}^{DCR}$ is the average $P_{G_{Slope}}$ of *DCR* pulses.

Secondary, or correlated, noise is due to the optical cross-talk and the afterpulsing induced by a primary avalanche previously generated by a noise source or by detected light photons. During the primary avalanche multiplication process, photons can be emitted due to hot carrier luminescence phenomena [26]. These photons may lead to:

- *Prompt optical cross-talk*, due to photons starting secondary avalanches in one or more neighbour μcells. Therefore, the prompt cross-talk probability P_{XT} can be expressed as:

$$P_{XT} = G \cdot P_{hv} \cdot P_G^{XT} \tag{14}$$

  where P_{hv} is the probability that a photons is emitted, reach the high field region of another μcell and create electron-hole pair, G is the SiPM gain, i.e. the number of charges created during primary avalanche multiplication (see Eq. 8) and P_G^{XT} is the average Geiger probability for cross-talk pulses. P_G^{XT} can be approximated as:

$$P_G^{XT} = 1 - e^{-P_{G_{Slope}}^{XT} \cdot \Delta V} \tag{15}$$

  where $P_{G_{Slope}}^{XT}$ is the average $P_{G_{Slope}}$ of cross-talk pulses.

- *Delayed optical cross-talk*, due to photons, absorbed in the non-depleted regions of the device (i.e. substrate), producing charge carriers that can drift through the depleted region and trigger secondary avalanches [27, 28]. The carrier diffusion time determines the delay time.

[8] https://www.silvaco.com/products/tcad.html

Afterpulsing occurs when, during the primary avalanche multiplication process, carriers are captured by trap levels in the μcell junction depletion layer and are released after some time, triggering a secondary avalanche discharge correlated to the primary one. Therefore, the afterpulse probability P_{AP} can be approximated as:

$$P_{AP} = G \cdot P_{trap} \cdot P_G^{P_{AP}}, \tag{16}$$

where P_{trap} is the probability that a carrier will be trapped and released after and $P_G^{P_{AP}}$ is the average Geiger probability for afterpulses.

Since, the afterpulsing occurs in the same μcell as primary avalanche, its amplitude A_{AP} strongly depends on the recovery state of the μcell, and can be expressed as:

$$A_{AP} = A_{1p.e.} - A_{1p.e.} \cdot \exp\left[-\frac{t}{\tau_{rec.}}\right], \tag{17}$$

where A_{1pe} is the single photoelectron (p.e.) amplitude and $\tau_{rec.} = R_q \cdot C_{\mu cell}$ is the recovery time constant.

As mentioned before, the device is considered as operated in dark conditions, in the time window of about 5 μs preceding the LED trigger. This time interval is used to calculate the dark count rate DCR.

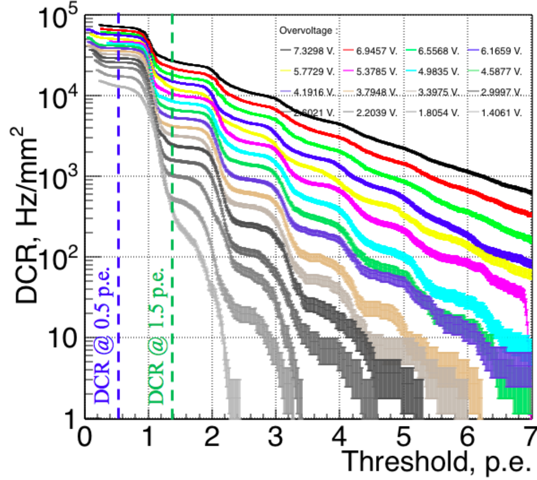

Figure 14: DCR vs. threshold for different values of overvoltage ΔV for the Hamamatsu S10943-2832(X) SiPM. The blue and green vertical lines represent the DCR at 0.5 p.e. and 1.5 p.e. thresholds, respectively.

The DCR as a function of a discriminating threshold expressed in photoelectrons $p.e.$ at a given ΔV is calculated by counting the number of SiPM pulses with amplitude above the threshold (see Fig. 14). This *counting* method is affected by afterpulses. To overcome this limitation, the Poisson statistic can be used to calculate pure uncorrelated SiPM noise at 0.5 p.e. threshold as:

$$DCR_{Poisson} = -\frac{ln\left(P_{dark}(0)\right)}{L} = -\frac{1}{L} ln\left(\frac{N_{dark}(0)}{N_{dark}(total)}\right) \tag{18}$$

where $P_{dark}(0)$ is the Poisson probability not to have any SiPM pulse and then $-ln(P_{dark}(0))$ is the average number of detected SiPM pulses within the time interval L. The $P_{dark}(0)$ can be calculated as:

$$P_{dark}(0) = -\frac{N_{dark}(0)}{N_{dark}(total)}, \tag{19}$$

where N_{dark}(total) represents the total number of analyzed waveform and $N_{dark}(0)$ is the number of waveforms without any SiPM pulse within given time interval L. As can be seen in Fig. 15, the $DCR_{Poisson}$ is overestimated for short window lengths (≤ 1 μs), as it also affected by afterpulses. So to estimate correctly the DCR, we need to use a window greater than 1 μs, where the DCR becomes flat within the error bars. This value clearly depends on the afterpulse probability and their distribution in time for the specific device, but the same method can be used to identify the right window size for any type of device.

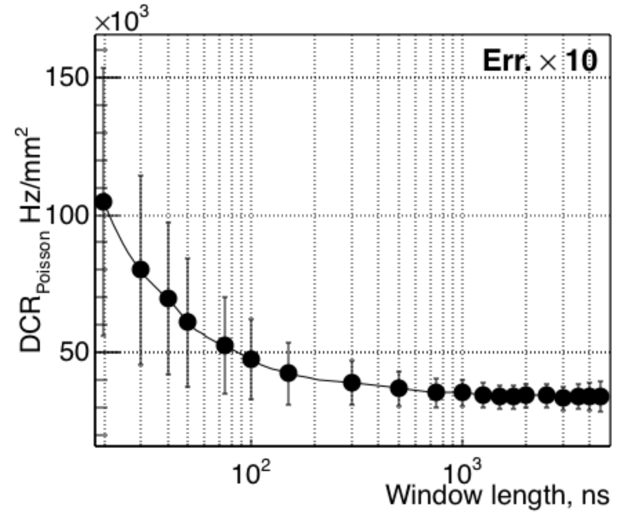

Figure 15: DCR calculated from Poisson statistics vs analysis window length.

Despite the fact that DCR calculated from pulse counting method is slightly overestimated due to afterpulses (see Fig. 16), it is anyhow interesting to use it to extract other important parameters of the device.

The trend of the DCR measured as function of the overvoltage, at the threshold of 0.5 p.e., can be fitted using Eq. 11. From the fit, we can extract $P_{G_{Slope}}^{DCR} = 0.366$ using Eq. 13 (for a physical interpretation of this parameter see Sec. 5.3). The discrepancy between data and fit is larger than the errors. This can be related to the fact that the fit formula does not include afterpulses and delayed optical cross-talk. The inclusion of these two effects would make the fit more complex and unstable. This inclusion is not worth given that the errors are quite small (10 ppm at $\Delta = 1.5$ V) and then the discrepancy has negligible impact.

4.5.1. *Prompt cross-talk probability*

The measured DCR at thresholds ≥ 1.5. p.e. can be regarded as the results of the optical cross-talk effects related to the $DCR_{0.5\ p.e.}$ and then

$$DCR_{1.5\ p.e.} = DCR_{0.5\ p.e.} \times P_{XT}, \tag{20}$$

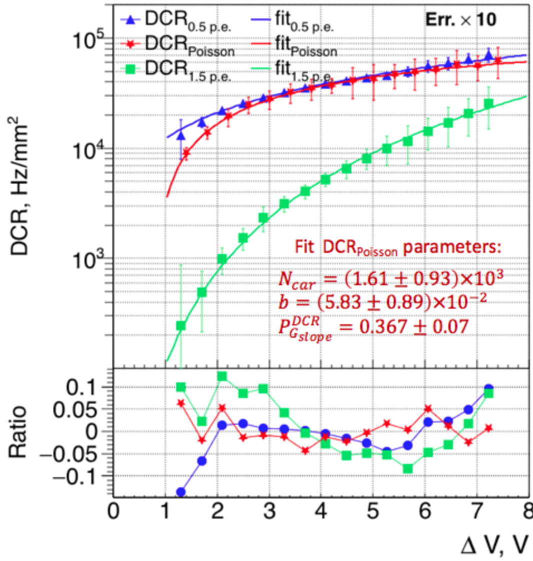

Figure 16: DCR vs. ΔV for Hamamatsu S10943-2832(X) for the 0.5 p.e. counting method (blue) as well as from Poisson statistics method (red) and the 1.5 p.e. threshold (green). Also, the difference between the experimental data and the fit, normalized to experimental data, is presented for the 0.5 (blue), 1.5 (green) p.e thresholds and Poisson statistics (red) are shown. The Fit parameters for the Poisson statistics method are indicated.

which can be used to define how to measure P_{XT}:

$$P_{XT} = \frac{DCR_{1.5p.e.}}{DCR_{0.5p.e.}}. \tag{21}$$

However also the pile up effect is present. The total rate of pile up pulses within a given time interval τ can be calculated as the sum of the pile up rate of two, three, four and more pulses ($R_{total} = R_{2p} + R_{3p} + R_{4p} + ...$). Using a standard approach [29], the rate for the estimation of accidental pile up of 2 pulses, with a rate of $DCR_{0.5p.e.}$ and a coincidence window of τ, is $2 \cdot \tau \cdot DCR^2_{0.5p.e.}$. Therefore, the total rate, R_{total}, for any number pile-up event, can be regarded as a geometrical series of $\tau \cdot DCR_{0.5p.e.}$:

$$\begin{aligned} R_{total} &= R_{2p} + R_{3p} + R_{4p} + ... \\ &= 2 \cdot \tau \cdot DCR^2_{0.5p.e.} + 2 \cdot \tau^2 \cdot DCR^3_{0.5p.e.} + ... \\ &= \frac{2 \cdot \tau \cdot DCR^2_{0.5p.e.}}{1 - \tau \cdot DCR_{0.5p.e.}} \end{aligned} \tag{22}$$

The P_{XT} can be corrected for the pile up effect as:

$$P^{Corrected}_{XT} = \frac{DCR_{1.5p.e.} - R_{total}}{DCR_{0.5p.e.} + R_{total}}. \tag{23}$$

In our case, the afterpulses can be neglected as they can appear within $\tau = 10\ ns$, and then their contribution to the amplitude is negligible. As matter of fact, the maximum possible afterpulse amplitude within this time interval was calculated from Eq. 17 and it is only 0.37 p.e. Therefore, the amplitude of the primary pulse, even including afterpulses, is still below 1.5 p.e. threshold.

In Fig. 17 the prompt optical cross-talk probability, P_{XT}, as a function of the over-voltage, ΔV, is shown (blue dots) together with the corrected one (green dots). The pile-up correction is below 1% due to the small value of τ, which is the minimal separation in time between two pulses needed for the automatic data analysis to recognize them as single pulses inside a train. However, the pile-up correction may become important when SiPMs with very low P_{XT} are used or when τ is much longer, as shown in Ref. [30].

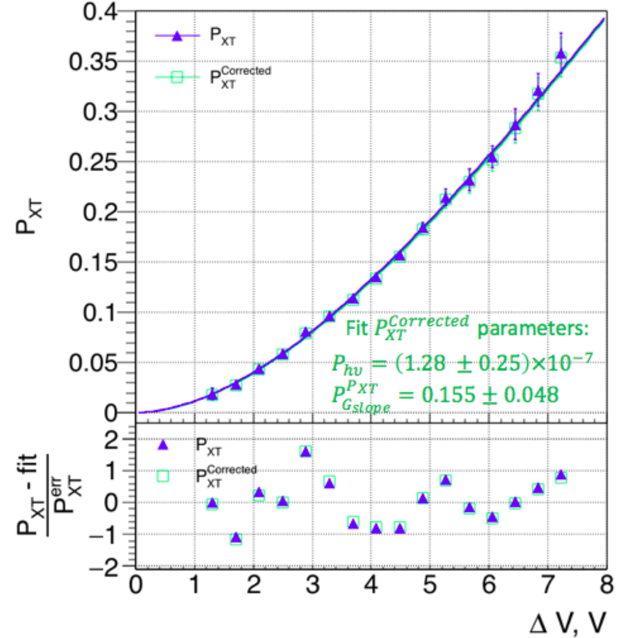

Figure 17: P_{XT} vs ΔV of Hamamatsu S10943-2832(X) with ($P^{Corrected}_{XT}$ in green) and without correction for the pile up effect (P_{XT} in blue). In the bottom plot the difference between experimental data and fit normalized to data errors is shown.

We can see that except for two points, the difference between fit and data is inside the error bars. Given $C_{\mu cell} = 85$ fF (See Tab. 1), two free parameters can be extracted from the fit of $P^{Corrected}_{XT}$: $P_{h\nu}$ and $P^{P_{XT}}_{G_{Slope}}$. We find an average probability $P_{h\nu} = 1.28 \times 10^{-7}$ that photon with sufficient energy can be emitted by one carrier crossing the junction during avalanche multiplication and reach the high field region of another μcell. Taking into account that the average probability of photons with energy higher than 1.14 eV (or $\lambda \leq 1000\ nm$), emitted by carriers crossing the junction, is 2.9×10^{-5} [31], we can conclude that around 2% of emitted photons reach the high field region of neighbouring μcells. The parameter $P^{P_{XT}}_{G_{Slope}} = 0.155$ is extracted from the fit. Its physical interpretation will be discussed later in section 5.3.

As a further cross-check, we use the value found here for P_{XT} to fit the data in Fig. 16 using Eq. 20 and Eq. 14. The parameters found from the fit of $DCR_{0.5\ p.e.}$ in Fig. 16 are fixed in the fit for $DCR_{1.5\ p.e.}$. Also in this case, the data are well reproduced by the fitted model, as for $DCR_{0.5\ p.e.}$

The P^{DCR}_{G}, extracted from DCR data shown in Fig. 16, rep-

resents the probability that a free carrier initiates an avalanche (see Eq. 11), while P_G^{XT} represents the probability that a photon (emitted by hot carrier luminescence) is absorbed and initiate an avalanche (See Eq. 14). In general, free carriers and luminescence photons are absorbed at different depths of SiPM active areas. Therefore, $P_G^{DCR} \neq P_G^{XT}$, even if they have a similar behaviour as a function of ΔV.

4.5.2. Afterpulse and delayed cross-talk probability

The afterpulse probability is measured by acquiring 20 μs long waveforms, triggering their acquisition and using a pulse with an amplitude larger than 0.5 p.e.. This pulse, called in the following primary pulse, is adjusted to fall in the center of the waveform (i.e. at 10 μs). To ensure that pulses are either afterpulses related to the primary pulse or randomly generated dark pulses, waveforms without any signal within the 5 μs preceding the primary pulse are selected and analyzed in the following. For all waveforms triggered by a primary signal of 1 p.e. amplitude, the time difference between primary pulse and first following pulse is shown in Fig. 18. The number of DCR pulses, separated by a given time difference Δt, can be calculated as:

$$N_{DCR}(\Delta t) = \frac{n_{DCR}}{\tau_{DCR}} \cdot exp\left(\frac{-\Delta t}{\tau_{DCR}}\right), \tag{24}$$

where $\tau_{DCR} = 1/DCR$ is the average time difference between two dark pulses and n_{DCR} is the normalization amplitude. Not to include afterpulses, the DCR from the Poisson statistics method was used. Eq. 24 is used to fit the data in Fig. 18, where the contribution due to the afterpulse component is also shown. This afterpulse component can be approximated as:

$$N_{AP} = \frac{n_{AP}}{\tau_{AP}} \cdot exp\left(\frac{-\Delta t}{\tau_{AP}}\right) \cdot \left(1 - exp\left(-\frac{\Delta t}{\tau_{rec.}}\right)\right), \tag{25}$$

where τ_{AP} is the afterpulse time constant and n_{AP} is the normalization amplitude, $1 - exp\left(-\frac{\Delta t}{\tau_{rec.}}\right)$ takes into account decreases of Geiger probability due to micro-cell recovery time. More than one afterpulse time constant (e.g. fast and slow) can presented, as shown in Ref. [22] for older SiPM devices. For the studied SiPM, a single τ_{AP} was found. This is due to the use of improved materials and wafer process technologies [11] reducing drastically afterpulses. Both Eq. 24 and Eq. 25 have similar exponential behavior, even if they are related to different physical phenomena: Poisson statistics of SiPM uncorrelated noise (Eq. 24) and SiPM trap level lifetime (Eq. 25).

The data in Fig. 18 are approximated as the sum of the 2 components:

$$N_{total}(\Delta t) = N_{DCR}(\Delta t) + N_{AP}(\Delta t). \tag{26}$$

This equation neglects the probability $P_{cor}(DCR, AP)$ that afterpulse and DCR pulse may appears in the same micro-cell within the micro-cell recovery time $5 \times \tau_{rec.}$ [32], since it is negligibly small:

$$P_{cor}(DCR, AP) = \frac{< DCR >}{N_{\mu cell}} \cdot 5 \times \tau_{rec.} \sim 2.5 \times 10^{-5}. \tag{27}$$

where $< DCR >$ is average DCR over ΔV at a given T.

Using this approximation to fit the data, the τ_{AP} can be extracted. It is shown in Fig. 19 as function of ΔV. Data for $\Delta V < 3V$ are not presented in Fig. 19 due to the very low afterpulse probability leading to poor statistics. The τ_{AP} is a device structure parameter depending on the SiPM structure, Si impurities and temperature. Therefore, variations of τ_{AP} with ΔV reflect measurements uncertainties. An average value of $< \tau_{AP} >$ of 6.769 ± 0.110 ns is found.

The number of afterpulses $N_{AP}(\Delta t)$, calculated as the difference between the measured number of events and $N_{DCR}(\Delta t)$, is represented by the blue histogram in Fig. 18. Then the afterpulse probability is calculated as:

$$P_{AP} = \frac{\int_0^{5\times<\tau_{AP}>} N_{AP}(\Delta t)dt}{N_{prim.}}, \tag{28}$$

where $N_{prim.}$ is the number of primary avalanches. The P_{AP} as a function of ΔV is presented in Fig. 19.

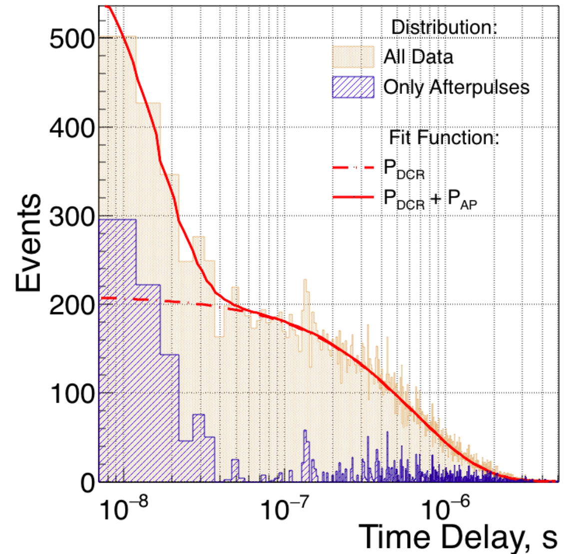

Figure 18: Distribution of the time difference between primary pulse and first following pulse at $\Delta V = 3.5$ V. By subtracting the contribution from DCR (dashed line), the distribution for afterpulses only (blue) was obtained.

Fig. 20 is a two-dimensional histogram of the amplitude in p.e. of the first pulse following a primary pulse of 1 p.e. vs the time difference between the two. This plot shows the various SiPM noise components. The population of dots around amplitude of 1 p.e and time delay larger than 50 ns are typically dark pulses and afterpulses. Nonetheless, for this device only dark counts contribute due to the short afterpulse time constant τ_{AP}. The population with amplitude lower than 1 p.e. and delay smaller than 50 ns are afterpulses produced when the μcell has not yet recovered. The population at time delay less 50 ns and amplitude 1 p.e. might be mostly delayed optical cross-talk, and some dark pulses or afterpulses related to avalanches happened more than 5 μs before the primary avalanche. The other

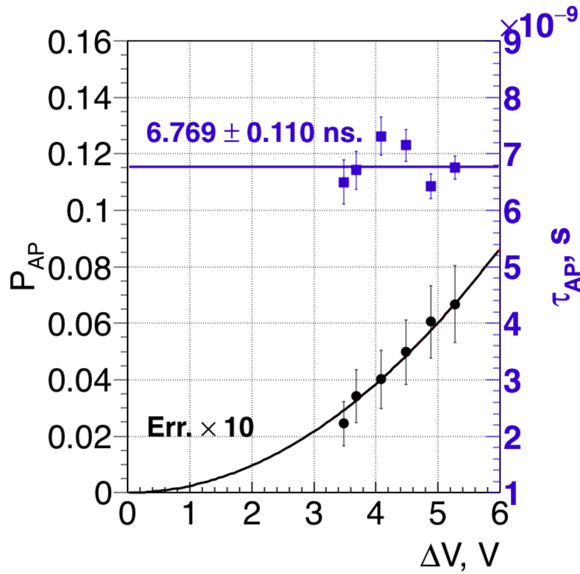

Figure 19: The P_{AP} and τ_{AP} as a function of ΔV. The afterpulse average time constant $< \tau_{AP} >$ of 6.769 ± 0.110 ns is found.

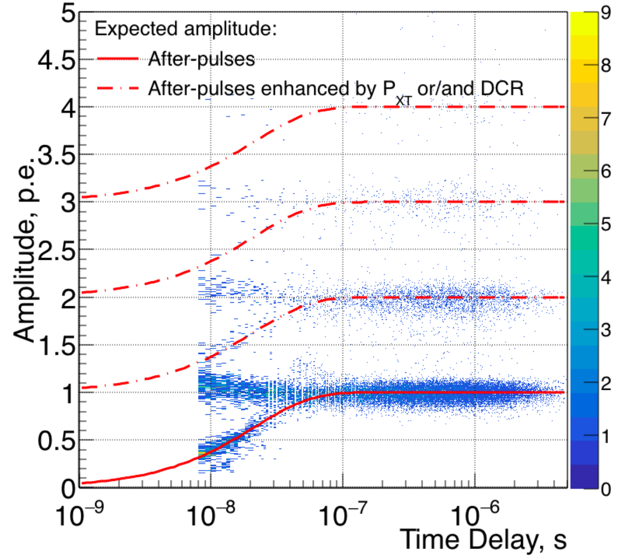

Figure 20: The 2D histogram shows the time difference between primary pulses and following ones on the x-axis and the amplitude of the second signal on the y-axis. The colors represent the number of events in each bin. The expected afterpulse amplitudes as a function of the delay time is calculated from the μcell recovery time for pure afterpulses (red solid line) and for enhanced afterpulses by optical cross-talk or dark pulses (dashed red lines).

populations at larger amplitude than 1 p.e. are of similar nature than what described for 1 p.e. but further enhanced by optical cross-talk. In the plot, the red solid line is calculated from Eq. 17 and the dashed lines are enhanced by optical cross-talk.

5. Optical characterisation

The photon detection efficiency (PDE) is one of the most important parameters describing the sensitivity of a SiPM as a function of wavelength of the incident light λ and the applied over-voltage ΔV: $PDE = QE(\lambda) \times \epsilon \times P_G(\Delta V, \lambda)$, where $QE(\lambda)$ is the quantum efficiency, P_G is the Geiger probability, and ϵ the μcell fill factor (the percentage of it that is sensitive to light). More details about each PDE component can be found in the Ref. [28]. To study the PDE, our experimental setup at IdeaSquare at CERN was used (see Fig. 21). In this Section, the methods used for both absolute (at a given λ) and relative (λ-dependent) PDE measurement are reported and corresponding results discussed at the end of the section.

5.1. Absolute PDE measurements with pulsed light

The schematic layout of the experimental set-up developed for absolute PDE measurements is shown in Fig 21a. The set-up is built around an integration sphere[9], used to produce at each output port a diffuse light of similar intensities by multiple scattering reflections on its internal surface. This destroys any spatial information of the incoming light usually produced by a LED but preserves the power at each port. A calibrated photodiode[10], placed on one output port, is used to determine the absolute amount of light scattered in the ports (power density), in order to estimate the number of photons impinging on the SiPM under test, sitting on the other port. The LED bias is provided by a pulse generator, with repetition rate of f = 500 Hz, chosen to:

- have reasonable acquisition time (∼ 45 min) for a full scan of the over-voltage in the range of 1 V ≤ ΔV ≤ 8 V with a step of 0.4 V, for each given wavelength;
- have a photocurrent level ($I \geq$ 100 pA) at least 50 times higher than the SiPM dark photocurrent;
- not saturate the LED, which exhibits a non linear behaviour for f > 3 kHz.

The dynamic range of the SiPM[11] is much lower than the one of a generic photodiode. To be able to illuminate the SiPM with different light intensities, a Neutral Density Filter[12] (*ND Filters*) is inserted between the integration sphere output port and the SiPM. To enable easy and fast replacement, the *ND Filter* is mounted on a motorized wheel. To uniformly illuminate the SiPM full active area, a 50° × 50° diffuser[13] is

[9] Thorlab, Model IS200-4

[10] Hamamatsu S1337-1010BQ, s/n 61

[11] The dynamic range is the range where SiPM signal charge is linearly proportional to number of photons. As matter of fact, the SiPM linearity relies on the fact that each photon hits a different μcell and the signal is the sum of the charge of the fired μcells. If the density of photons is too high, the probability that a photon impinges on a μcell, which has been already fired, and thus is inactive, becomes non negligible. In this case, not all photons contribute to the signal and then the linearity is lost and the device is said to be saturated.

[12] Thorlab, Model NE530B

[13] Thorlab, ED1-S50-MD

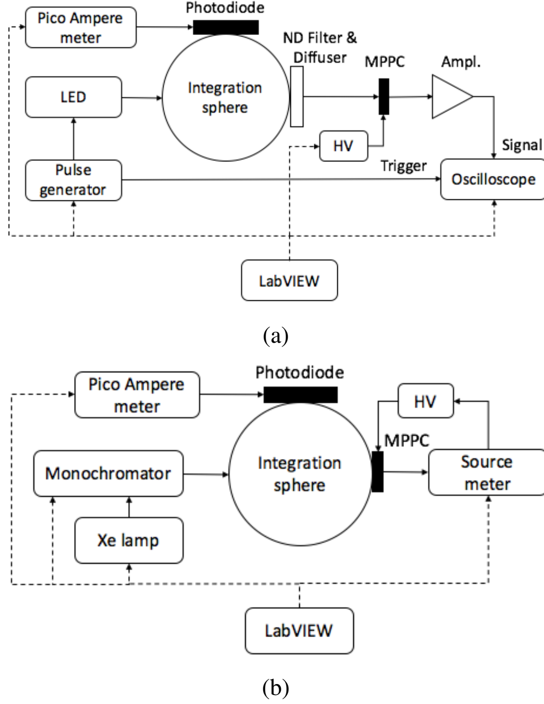

Figure 21: Schematic layouts of the developed experimental set-up for: absolute 21a and relative 21b *PDE* measurements

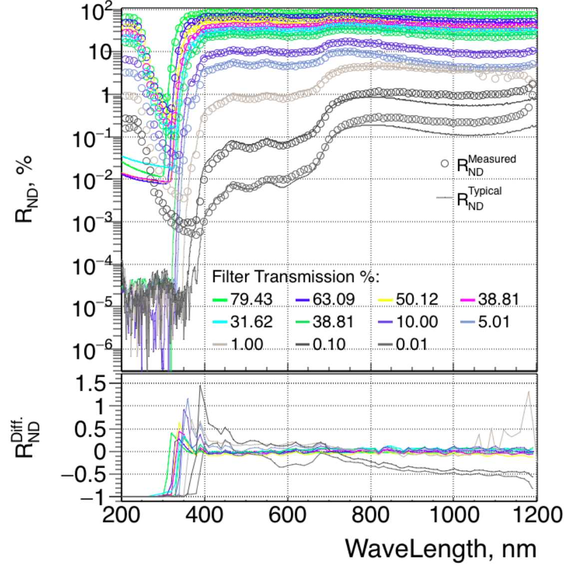

Figure 22: Measured (open dots) $R_{ND}^{Measured}(n)$ and "typical" one $R_{ND}^{Typical}(n)$ given by producer (lines) transmission of ND Filters as a function of wavelength. In the bottom pane, it is shown the relative differences $R_{ND}^{Diff.}(n)$ as defined in the text.

mounted after the *ND Filter*. The surface uniformity is measured using a LED ($\lambda = 405$ nm), and a small photodiode[14] (with 0.8 mm^2 active area) mounted on a 2D translation stage[15]. The light intensity non-uniformity, which has also to be taken into account for the *PDE* calculation, was measured over the active area of the hexagonal SiPM and it is < 2%.

The power ratio, $R = P_{PD}/P_{SiPM}$, between the light intensity measured by the calibrated photodiode, P_{PD}, and the SiPM, P_{SiPM}, is measured experimentally as described in Ref. [33]. Measurements were done for different light wavelengths (i.e. 405, 420, 470, 505, 530, 572 nm).

The transparency ($R_{ND}(n)$) of the *ND Filter* n at a given λ is measured as:

$$R_{ND}(n) = \frac{I_{ND}(n)}{I_{PD}} \cdot \frac{1}{R_{Geom.}}, \tag{29}$$

where n is the *ND Filter* number ($n = 1$ is used when there is no filter); $I_{ND}(n)$ and I_{PD} are the photocurrents measured by one photodiode positioned after the *ND Filter* and the reference photodiode positioned at another output of the integration sphere, respectively; $R_{Geom.} = \frac{I_{ND}(n=1)}{I_{PD}}$ is the power ratio between the light intensity measured by the photodiodes when there is no *ND Filter*. In order to measure R_{ND}, a Xenon lamp (75 W) was coupled with a monochromator[16] to select λ. The comparison between the measured values, $R_{ND}^{Measured}(n)$, and the "typical" one given by the producer, $R_{ND}^{Typical}(n)$, as a function of λ and for different attenuation filters is presented in Fig. 22 together with the relative differences, on bottom of the figure.

The data acquisition system is similar to the one presented in Sec. 4.1. During data taking, the photocurrent of the photodiode is read out by the Keithley 6487. Data taking is triggered by a pulse generator and controlled by a Labview program to automate the necessary measurement steps.

The absolute *PDE* is calculated using the so-called Poisson method [22, 34, 33, 28] from the average number of detected photons, corrected by factor k_{LED}^{corr} to take into account the uncorrelated SiPM noise:

$$\begin{aligned} k_{LED}^{corr} &= -\ln\left(P_{LED}(0)\right) + \ln\left(P_{dark}(0)\right) \\ &= -\ln\left(\frac{N_{LED}(0)}{N_{LED}(total)}\right) + \ln\left(\frac{N_{dark}(0)}{N_{dark}(total)}\right), \end{aligned} \tag{30}$$

where $N_{dark}(0)$ and $N_{dark}(total)$ are the number of waveforms with no SiPM signal within the *dark* regions preceding it and the total number of recorded waveforms, respectively.

The *PDE* can be calculated as:

$$PDE = \frac{k_{LED}^{corrected}}{N_{ph}}, \tag{31}$$

where N_{ph} is the average number of photons hitting the SiPM. The N_{ph} can be estimated from converting the photocurrent from the calibrated photodiode as:

$$N_{ph} = \frac{I_{PD} \times R \times R_{ND} \times \alpha_{light}}{f \times QE_{PD}(\lambda) \times e}, \tag{32}$$

[14] Thorlab, Model SM05PD2A

[15] two Thorlab LTS300 motorized stages connected together by Z-Axis bracket.

[16] Oriel Tunable Light Source System TLC-75X

where I_{PD} is the photocurrent measured by the calibrated photodiode, $QE_{PD}(\lambda)$ is the photodiode quantum efficiency, f is the pulse repetition frequency (typically $f = 500\ Hz$) and e is the electron charge. The PDE as a function of ΔV for six different wavelengths is shown in Fig. 23. There are three main sources of uncertainty for the PDE determination:

- The precision on N_{ph}, calculated from the photodiode current, used for its calibration curve, and corrected by the power ratio $R = P_{PD}/P_{SiPM}$.
- The determination of k^{corr}_{LED} based on the separation of the "0 p.e." and "1 p.e." peaks, affected by SiPM noise (i.e. DCR, P_{XT} and P_{AP}), which are proportional to the "*LED*" *gate*.
- The precision of the calibrated quantum efficiency curve of the photodiode.

Therefore, for precise absolute *PDE* measurements perfectly calibrated photodiodes, fast LEDs or lasers are strongly preferable. In the Fig. 23, we can observe that the error bars are different for different wavelengths. This reflects the variations of the LED light intensity during the measurements, which determine the precision of k^{corr}_{LED} calculation.

The *PDE* of a SiPM can be obtained fitting the data as a function of ΔV (see Fig. 23) for each wavelength with the function:

$$PDE = PDE_{max} \times P_G \quad (33)$$

where P_G is the Geiger probability (See. Eq. 12) and PDE_{max} is a free parameter, which depends on SiPM type, light wavelength and to some extent on temperature [25]. Such a parameterisation provides a good description of our experimental data as shown in Fig. 23.

5.2. Relative PDE measurement with continuous light

The absolute *PDE* measurements method requires a pulsed light source, as LEDs or a laser, so it is possible only for a limited number of wavelengths. Therefore, to measure the *PDE* in a wide wavelength range, from 260 nm up to 1150 nm, a second method, the so called "Relative PDE", is used. The schematic layout of the experimental set-up developed for the relative *PDE* measurement is shown in Fig 21b. The reverse current-voltage IV characteristics of the SiPM device at different wavelengths are performed using a Keithley 2400, while a Keithley 6487 is used to read photocurrent from calibrated photodiode.

The collection of reverse IV curves of the Hamamatsu S10943-2832(X) SiPM, for different wavelengths from 260 nm up to 1150 nm, is shown in Fig. 24. The difference between SiPM current with light and in dark condition $I^{light}_{SiPM} - I^{dark}_{SiPM}$ at a given ΔV can be expressed as:

$$I^{light}_{SiPM} - I^{dark}_{SiPM} = PDE(\Delta V, \lambda) \times N_\gamma \times e \times G^{eff.}_{SiPM}(\Delta V), \quad (34)$$

where $PDE(\Delta V, \lambda)$ is the *PDE* at a given ΔV and λ, N_γ is the average number of photons sent to the SiPM device per given

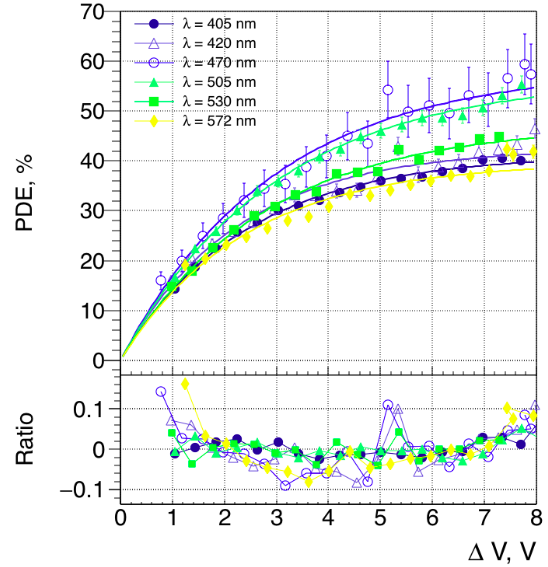

Figure 23: *PDE* vs. ΔV of the Hamamatsu S10943-2832(X) SiPM. The results are presented for six different wavelengths: 405 nm, 420 nm, 470 nm, 505 nm, 530 nm and 572 nm. Also, the $Ratio = \left(PDE_{data} - PDE_{fit}\right) \div PDE_{data}$ is shown.

time interval, $G^{eff.}_{SiPM}(\Delta V)$ is the effective SiPM gain, namely the SiPM gain enhanced by cross-talk and afterpulses effects (for more details see Sec. 4.1). The N_γ is proportional to the photocurrent from the calibrated photodiode $I_{PD}(\lambda)$. Therefore, the relative *PDE* in Eq. 34 can be rewritten as:

$$PDE(\Delta V, \lambda) = \frac{I^{light}_{SiPM} - I^{dark}_{SiPM}}{e \times N_{p.e.} \times G^{eff.}_{SiPM}(\Delta V)} \propto \frac{I^{light}_{SiPM} - I^{dark}_{SiPM}}{I_{PD}(\lambda)} \quad (35)$$

The relative *PDE* as a function of λ at $\Delta V = 2.8$ V is presented in Fig. 25, together with the values as calculated from the "IV Model" (see Sec. 3.2) by re-normalising them to the light intensity as estimated with the calibrated photodiode.

At a given temperature, the $C_{\mu cell}$ and dN_{car}/dt of a SiPM device do not depend on light intensity, but only on the SiPM internal structure. Therefore, a simultaneous fit is done assuming that $C_{\mu cell}$ and $\frac{dN_{car}}{dt}$ are the same for all curves. To reduce computing time, the fit procedure used only eight curves corresponding to 300, 350, 400, 470, 550, 600, 700 and 800 nm wavelengths. The relative *PDE* calculated from the "IV Model" is in good agreement with the results calculated from Eq. 35, as shown in Fig. 25. The main advantage of the "IV Model" for relative *PDE* calculation is that also the breakdown voltage is extracted from the fit. As a matter of fact, in Eq. 35 the currents are measured as function of V_{bias} and then to derive the *PDE* vs over-voltage, the V_{BD} has to be known or determined independently.

To have an absolute *PDE* vs λ, the relative *PDE* is normalised to the absolute values obtained from Eq.33 at $\Delta V = 2.8$ V and presented in Fig. 26. Due to the complicated behaviour of the *PDE* vs λ, a sum of three polynomial functions

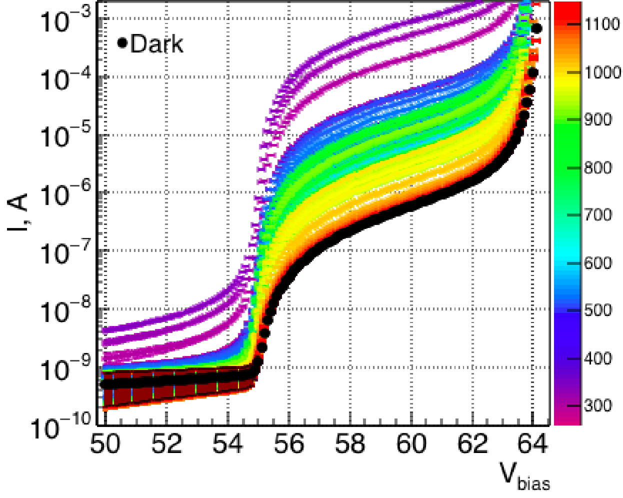

Figure 24: The reverse IV measurements of the Hamamatsu S10943-2832(X) SiPM illuminated by continuous light for various wavelengths from 260 nm up to 1150 nm. and in dark (black dots). The colors represent the wavelengths

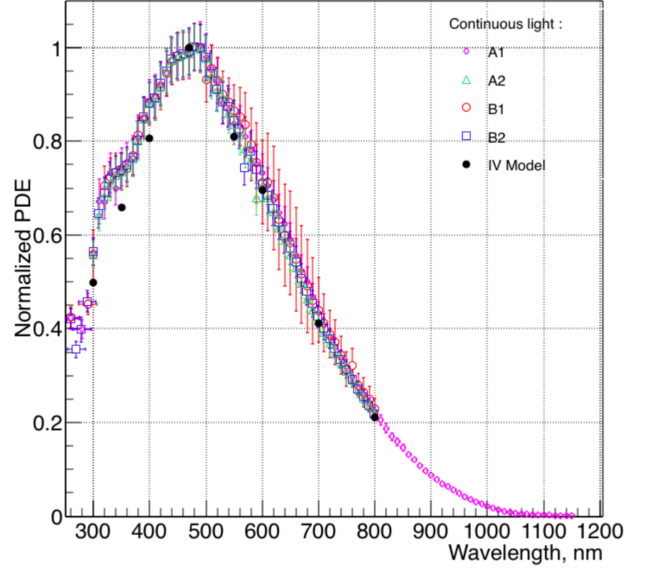

Figure 25: The relative PDE vs λ for the Hamamatsu S10943-2832(X) SiPM. The results are presented for all four channels: A1, B1, A2, B2 and also for the PDE calculated from the "IV Model" for the channel A1 (black points).

is used to fit the experimental data from 260 up to 1000 nm:

$$\begin{aligned} PDE(\lambda) &= \left(a_1 + b_1\cdot\lambda + c_1\cdot\lambda^2\right)\cdot\mathcal{H}_1(\lambda) \\ &+ \left(a_2 + b_2\cdot\lambda + c_2\cdot\lambda^2\right)\cdot\mathcal{H}_2(\lambda) \\ &+ \left(a_3 + b_3\cdot\lambda + c_3\cdot\lambda^2 + d_3\cdot\lambda^3\right)\cdot\mathcal{H}_3(\lambda), \end{aligned} \quad (36)$$

where a_i, b_i, c_i, with $i = 1, 2, 3$, and d_3 are free parameters and $\mathcal{H}_i$ are Heaviside step functions in the ranges:
$\mathcal{H}_1$: 260 nm $< \lambda <$ 370 nm, $\mathcal{H}_2$: 370 nm $< \lambda <$ 530 nm,
$\mathcal{H}_3$: 530 nm $< \lambda <$ 1000 nm.

The result in Fig. 26 shown a good agreement between experimental data and the fit using Eq. 37.

The PDE as a function of ΔV and λ is particularly useful to predict its variations with experimental conditions, such as temperature or the NSB [35], which affects ΔV and then the sensor response. The PDE as a function of ΔV and λ, shown in Fig. 27, can be obtained by combining the the absolute and relative PDE measurements.

The analytical expression of the PDE is given in Eq. 33. As can be seen in Fig. 28, data and this representation agree within 3% on average. At low over-voltages ($\Delta V \leq 1.5$ V), there is the largest disagreement between the fit function and the data:

- $\lambda \leq 300$ nm, the Xe lamp was operated with a larger slit width of 1.24 mm, to have enough light. As consequence, the wavelength resolution was of 16.1 nm and this resulted in lower precision on PDE (See Fig. 26) and then in a worse quality fit;

- for $\lambda \geq 800$ nm, the photocurrent generated by the SiPM is comparable to its dark current (see Fig. 24) and, therefore, the signal to noise ratio is low.

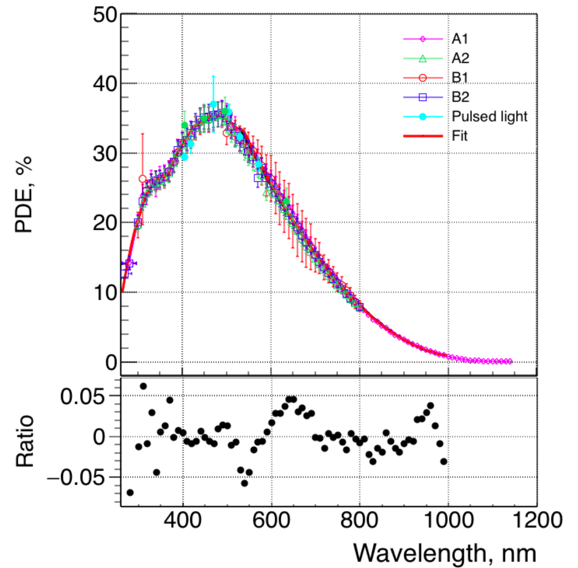

Figure 26: The PDE vs wavelength for the Hamamatsu S10943-2832(X) SiPM from 260 nm up to 1000 nm at $\Delta V = 2.8V$. Each channel is presented by a different colour and the PDE from pulsed light is presented by cyan dots. Also the fit is shown by the red line and the $Ratio = \left(PDE_{data} - PDE_{fit}\right) \div PDE_{data}$ is shown in the bottom plot.

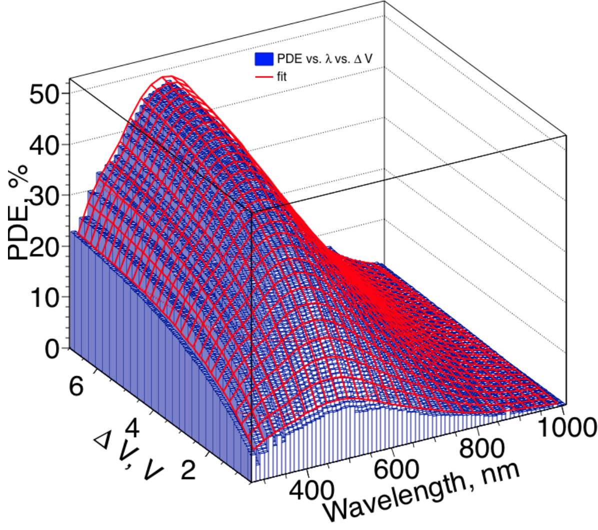

Figure 27: The PDE vs. λ and ΔV for S10943-2832(X).

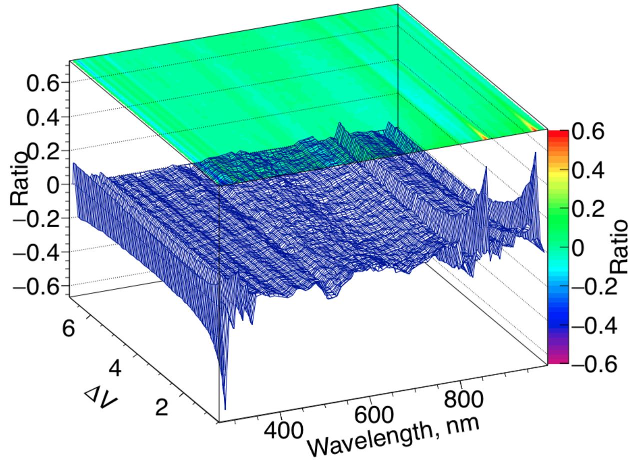

Figure 28: The difference between the measured PDE and the fit function divided by the measured PDE.

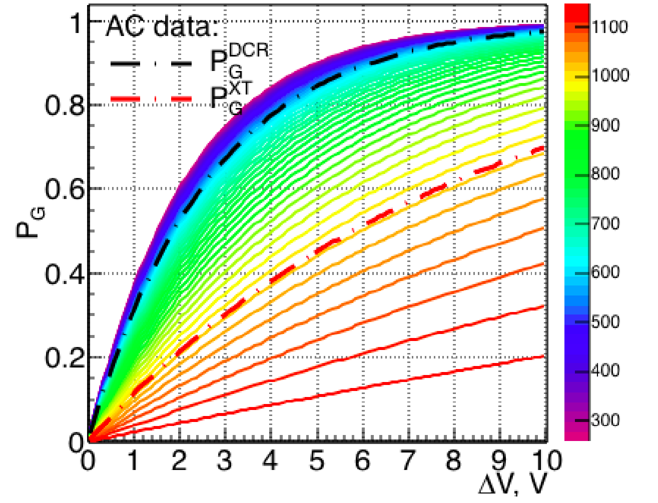

Figure 29: P_G as a function ΔV for various λ. The colors represent the wavelengths. Also the average P_G for DCR and for P_{XT} are shown.

5.3. Geiger probability

The Geiger probability P_G, also known as triggering probability, represents the probability that a carrier reaching the high field region will trigger an avalanche.

The P_G as a function of ΔV for different wavelengths λ is shown in Fig. 29, where it is evident how P_G increases with increasing ΔV much rapidly for short wavelengths (blue light). Oldham [36] and McIntyre [23] relate this behaviour to the properties of light absorption in silicon and to the SiPM μcell structure and ionisation rates of electrons, α_e. and holes, α_h. In particular, for $p^+/n/n-epi/n$-sub-structure P_G at short wavelengths λ (blue light) is dominated by α_e while at long one (red light) it is dominated by α_h. Thus, the fast increase of P_G with ΔV at short λ is related to the fact that $\alpha_e >> \alpha_h$ [37].

The average probabilities that thermal pulses (see Sec. 4.5) or pulses created by optical cross-talk (see Sec. 4.5.1) trigger an avalanche are indicated as P_G^{DCR} and P_G^{XT} in Fig. 29. As can be seen, P_G^{DCR} is equal to P_G (black dashed line) at $\lambda = 565$ nm and P_G^{XT} (red dashed line) is equal to P_G at $\lambda = 1041$ nm. From this and previously discussed behavior between λ and α_e, α_h we may conclude that:

- the main contribution of DCR is triggered by both electrons and holes;
- the main contribution of P_{XT} is triggered by holes;

6. Conclusions

In this work we report about the characterization measurements of the large area hexagonal SiPM S10943-2832(X). We measure all relevant SiPM parameters, detailed in Tab. 2. We also show how to build a PDE function of the wavelength and over-voltage. This is of paramount importance to determine the working point of SiPMs in real applications where external factors can affect its parameters, such as in the presence of NSB.

Additionally, we compare several methods commonly used for V_{BD} estimate from the reverse current voltage IV measurement. The functions to fit PDE, DCR P_{XT} and P_{AP} are discussed. We also show how, from these fits, the triggering probability P_G as function of the wavelength can be extracted. From its behaviour we infer that the DCR is triggered by both electrons and holes, while the cross-talk is initiated by avalanches triggered mainly by holes.

Breakdown voltage V_{BD}^{AC}	54.699 ± 0.017 ± 0.025 V
DCR/mm^2 @ $0.5 p.e.$ (@V_{op})	26.50 ± 0.15 KHz
DCR/mm^2 @ $1.5 p.e.$ (@V_{op})	1.735 ± 0.04 KHz
P_{XT} (@V_{op})	6.5 %
P_{AP} (@V_{op} within 5 μs)	< 2 %
PDE (@V_{op} & λ = 472 nm)	35.5 ± 3.5 %
Peak sensitivity wavelength	480 nm
Quenching resistor R_q	182.9 ± 0.3 ± 31. $k\Omega$

Table 2: S10943-2832(X) SiPM main measured characteristics at T = 25 °C. $V_{op} = V_{BD} + 2.8$ V.

Acknowledgements

This project has received funding from the European Union's Horizon 2020 research and innovation programme under grant agreement No 713171. Also, we acknowledge the support of the SNF funding agency. This paper has gone through internal review by the CTA Consortium.

References

References

[1] Y. Sun, J. Maricic, *SiPMs characterization and selection for the DUNE far detector photon detection system*, JINST 11 (01) (2016) C01078.
URL http://stacks.iop.org/1748-0221/11/i=01/a=C01078

[2] H. Anderhub, et al., *Design and Operation of FACT – The First G-APD Cherenkov Telescope*, JINST 8 (06) (2013) P06008–P06008. doi:10.1088/1748-0221/8/06/p06008.
URL https://doi.org/10.1088%2F1748-0221%2F8%2F06%2Fp06008

[3] M. Heller, et al., *An innovative silicon photomultiplier digitizing camera for gamma-ray astronomy*, The European Physical Journal C 77 (1) (2017) 47. doi:10.1140/epjc/s10052-017-4609-z.
URL https://doi.org/10.1140/epjc/s10052-017-4609-z

[4] J. Aguilar, et al., *Design, optimization and characterization of the light concentrators of the single-mirror small size telescopes of the Cherenkov Telescope Array*, Astrop. Phys. 60 (2015) 32. doi:{10.1016/j.astropartphys.2014.05.010}.

[5] J. Aguilar, et al., *The front-end electronics and slow control of large area SiPM for the SST-1M camera developed for the CTA experiment*, Nucl. Instrum. Meth. A 830 (2016) 219 – 232. doi:https://doi.org/10.1016/j.nima.2016.05.086.
URL http://www.sciencedirect.com/science/article/pii/S0168900216304788

[6] Series 2400 sourcemeter line.
URL http://www.testequipmenthq.com/datasheets/KEITHLEY-2400-Datasheet.pdf

[7] W. Shockley, *The Theory of p-n Junctions in Semiconductors and p-n junction Transistors*, Bell System Technical Journal (1949) 435–489.

[8] W. Shockley and W.T. Read, *Statistics of the Recombinations of Holes and Electrons*, Phys. Rev. 87 (1952) 835. doi:{10.1103/PhysRev.87.835}.

[9] E. H. Hall, *On a New Action of the Magnet on Electric Currents*, American J. of Math. 2 (3) (1879) 287.

[10] J. Frenkel, *On Pre-Breakdown Phenomena in Insulators and Electronic Semi-Conductors*, Phys. Rev. 54 (1938) 647. doi:10.1103/PhysRev.54.647.

[11] Hamamatsu Photonics K.K.Opto-semiconductor Handbook Editorial Committee, *Opto-semiconductor Handbook*, Hamamatsu Photonics K.K.Solid State Division (2014) 60–61.

[12] E. Garutti, M. Ramilli, C. Xu, W. L. Hellweg, R. Klanner, *Characterization and X-Ray Damage of Silicon Photomultipliers*, PoS TIPP2014 (2014) 070. doi:10.22323/1.213.0070.

[13] M. Simonetta, et al., *Test and characterisation of SiPMs for the MEGII high resolution Timing Counter*, Nucl. Instrum. Meth. A 824 (2016) 145. doi:10.1016/j.nima.2015.11.023.

[14] N. Ferenc, G. Hegyesi, K. Kalinka and J. Molnár, *A model based {DC} analysis of SiPM breakdown voltages*, Nucl. Instrum. Meth. A 849 (2017) 55. doi:https://doi.org/10.1016/j.nima.2017.01.002.

[15] N. Dinu, A. Nagai and A. Para, *Breakdown voltage and triggering probability of SiPM from IV curves at different temperatures*, Nucl. Instrum. Meth. A 845 (2017) 64, Proc. of the Vienna Conf. on Instr. 2016. doi:https://doi.org/10.1016/j.nima.2016.05.110.

[16] A. Nagai, N. Dinu, A. Para, *Breakdown voltage and triggering probability of SiPM from IV curves*, in: 2015 IEEE Nucl. Sci. Symp. and Med. Im. Conf., 2015, pp. 1–4. doi:10.1109/NSSMIC.2015.7581735.

[17] G. Bonanno, D. Marano, M. Belluso, S. Billotta, A. Grillo, S. Garozzo, G. Romeo, M. C. Timpanaro, *Characterization Measurements Methodology and Instrumental Set-Up Optimization for New SiPM Detectors Part I: Electrical Tests*, IEEE Sensors Journal 14 (10) (2014) 3557–3566. doi:10.1109/JSEN.2014.2328621.

[18] N. Serra et al., *Experimental and TCAD Study of Breakdown Voltage Temperature Behavior in n^+/p SiPMs*, IEEE Trans. on Nucl. Sci. 58 (3) (2011) 1233. doi:{10.1109/TNS.2011.2123919}.

[19] Z. Guoqing, H. Dejun, Z. Changjun and Z. Xuejun, *Turn-on and turn-off voltages of an avalanche pn junction*, J. of Semiconductors 33 (9) (2012) 094003.

[20] V. Chmill, E. Garutti, R. Klanner, M. Nitschke, J. Schwandt, *On the characterisation of SiPMs from pulse-height spectra*, Nucl. Instrum. Meth. A 854 (2017) 70 – 81. doi:https://doi.org/10.1016/j.nima.2017.02.049.
URL http://www.sciencedirect.com/science/article/pii/S0168900217302334

[21] A. Nagai, N. Dinu-Jaeger, A. Para, *Silicon Photomultiplier for Medical Imaging -Analysis of SiPM characteristics-* (2019). arXiv:1907.03926.

[22] P. Eckert, H.-C. Schultz-Coulon, W. Shen, R. Stamen, A. Tadday, *Characterisation studies of silicon photomultipliers*, Nucl. Instrum. Meth. A 620 (2) (2010) 217 – 226. doi:https://doi.org/10.1016/j.nima.2010.03.169.
URL http://www.sciencedirect.com/science/article/pii/S0168900210008156

[23] R. J. McIntyre, *Theory of Microplasma Instability in Silicon*, J. Appl. Phys. 32 (1961) 983.

[24] A. N. Otte, D. Garcia, T. Nguyen, D. Purushotham, *Characterization of three high efficiency and blue sensitive silicon photomultipliers*, Nucl. Instrum. Meth. A 846 (2017) 106 – 125. doi:https://doi.org/10.1016/j.nima.2016.09.053.
URL http://www.sciencedirect.com/science/article/pii/S0168900216309901

[25] G. Collazuol, M. Bisogni, S. Marcatili, C. Piemonte, A. D. Guerra, *Studies of silicon photomultipliers at cryogenic temperatures*, Nucl. Instrum. Meth. A 628 (1) (2011) 389 – 392, VCI 2010. doi:https://doi.org/10.1016/j.nima.2010.07.008.
URL http://www.sciencedirect.com/science/article/pii/S0168900210015500

[26] J. Bude, N. Sano, A. Yoshii, *Hot-carrier luminescence in Si*, Phys. Rev. B 45 (1992) 5848–5856. doi:10.1103/PhysRevB.45.5848.

URL https://link.aps.org/doi/10.1103/PhysRevB.45.5848

[27] C. Piemonte, A. Gola, *Overview on the main parameters and technology of modern Silicon Photomultipliers*, Nucl. Instrum. Meth. A 926 (2019) 2 – 15, silicon Photomultipliers: Technology, Characterisation and Applications. doi:https://doi.org/10.1016/j.nima.2018.11.119. URL http://www.sciencedirect.com/science/article/pii/S0168900218317716

[28] F. Acerbi, S. Gundacker, *Understanding and simulating SiPMs*, Nucl. Instrum. Meth. A 926 (2019) 16 – 35, silicon Photomultipliers: Technology, Characterisation and Applications. doi:https://doi.org/10.1016/j.nima.2018.11.118. URL http://www.sciencedirect.com/science/article/pii/S0168900218317704

[29] J. A. Grieve, R. Chandrasekara, Z. Tang, A. Ling, *Correcting for accidental correlations in saturated avalanche photodiodes*, Opt. Express 24 (2016) 3592–3600. arXiv:1509.03959, doi:10.1364/OE.24.003592.

[30] A. Nagai, et al., *SENSE: A comparison of photon detection efficiency and optical crosstalk of various SiPM devices*, Nucl. Instrum. Meth. A 912 (2018) 182 – 185, new Developments In Photodetection 2017. doi:https://doi.org/10.1016/j.nima.2017.11.018. URL http://www.sciencedirect.com/science/article/pii/S0168900217312044

[31] A.L. Lacaita et al., *On the bremsstrahlung origin of hot-carrier-induced photons in silicon devices*, IEEE Trans. on Elect. Devices 40 (1993) 577. doi:10.1109/16.199363.

[32] N. Dinu, et al., *Temperature and bias voltage dependence of the MPPC detectors*, in: IEEE Nucl. Sci. Symp. and Med. Im. Conf., 2010, pp. 215–219. doi:10.1109/NSSMIC.2010.5873750.

[33] A. Basili, J.A. Aguilar, A. Christov, D. della Volpe, T. Montaruli, M. Rameez, *Characterization of New Hexagonal Large Area MPPCs*, IEEE Trans. on Nucl. Sci. 61 (2014) 1474. doi:{10.1109/TNS.2014.2321339}.

[34] V. Chaumat, C. Bazin, N. Dinu, V. Puill, J.-F. Vagnucci, *Absolute photo detection efficiency measurement of silicon photomultipliers*, in: Proceedings of Science, 2012.

[35] J. Aguilar, et al., *Front-end and slow control electronics for large area SiPMs used for the single mirror Small Size Telescope (SST-1M) of the Cherenkov Telescope Array (CTA)*, Proc.SPIE 9915 (2016) 9915 – 9915 – 8. doi:10.1117/12.2232982. URL http://dx.doi.org/10.1117/12.2232982

[36] W. G. Oldham, R.R. Samuelson, P. Antognetti , *Triggering Phenomenain Avalanche Diodes*, IEEE Trans. on Elect. Devices 19 (1972) 1056–1060.

[37] C. R. Crowell, S. M. Sze, *Temperature Dependence of Avalanche Multiplication in Semiconductors*, Applied Physics Letters 9 (1966) 242–244. doi:10.1063/1.1754731.